GRAZING BIFURCATIONS AND CHAOS IN THE DYNAMICS OF A HYDRAULIC DAMPER WITH RELIEF VALVES*

R.D. EYRES†, P.T. PIIROINEN† , A.R. CHAMPNEYS† , AND N.A.J. LIEVEN†

Abstract. This paper numerically investigates the closed loop dynamics of a lumped mass attached to a linear spring and a nonlinear hydraulic damper with relief valves. The damper in question is designed to have piecewise linear characteristics. The inclusion of the nonlinear damper into the closed loop system leads to regions of periodic motion separated by regions of non-periodic dynamics as the forcing frequency changes. Analysis of the system uses discontinuous nonsmooth numerical continuation techniques to follow the stable and unstable solutions along with bifurcation diagrams to aid the understanding of the non-periodic dynamics. The impacting of the relief valves leads to grazing bifurcation analysis using discontinuity mappings that explains some 'corners' observed in the bifurcation diagram and predicts the onset of chaotic dynamics. Other nonsmooth events such as the grazing of an invariant torus are suggested by numerical simulations.

Key words. Grazing bifurcation, Nonlinear, Hydraulic damper, Valve

1. Introduction. This paper conducts a detailed bifurcation analysis of a model of a common design of hydraulic damper with relief valves, embedded in a simple closed loop. The model was derived by us in [11], based upon previous work by [26, 27] and shown to match with experimental data. The purpose of this paper is not to match experiments but to show how such a simple damper configuration, designed to produce an overall piecewise force-velocity characteristic can itself be responsible for undesirable, chaotic dynamics. It should be stressed that these dynamics occur at an entirely different range of frequencies from that envisaged in the design of the particular damper that inspired our study in [11]. Let us first explain some background.

Hydraulic dampers are used in many engineering applications that can vary from earthquake resistant buildings [13] to car shock absorbers [29]. The advantage of using a hydraulic damper compared to other kinds of damper, is that the force generated is a function of the input velocity, resulting in a force that is out of phase with displacement. For applications such as bridges and buildings this means the energy from the unwanted vibrations can be dissipated without introducing potentially destructive stress forces. A *passive* damper does not require any external control input and as such can only produce a motion-suppressing force. The damper studied in this paper does however have a nonlinear force-velocity characteristic which can cause unwanted non-periodic motion. It should be noted that in section 4 an *unstable* periodic solution implies the system will deviate to another solution given a perturbation. This is not the same as the whole system becoming unstable due to the damper. Such an unstable system could have dynamics such as unbounded growth of a displacement. This does not occur in the parameter range studied in this paper.

One of the primary reasons for modelling a system using physically-based parameters is to enable some degree of optimisation or improvements to the system without having to manufacture a new unit. However as suggested above, some parameter changes could lead to the system becoming unstable or unpredictable. This paper will focus upon the different types of dynamics that can result from a simple and currently used damper system. The parameter values chosen are typical of the damper

*Work supported by EPSRC and Westland Helicopters Limited, an AgustaWestland company.

†Bristol Laboratory for Advanced Dynamic Engineering, University of Bristol, Bristol, BS8 1TR, UK ({richard.eyres, petri.piiroinen, a.r.champneys, nick.lieven}@bristol.ac.uk).

studied in [11]. The varying parameter will be the forcing frequency of the system. The frequency range studied is not necessarily representative of any real system but displays dynamics that might occur at more realistic frequencies in other areas of parameter space.

1.1. Nonsmooth dynamical systems. Nonlinear dynamical systems can often be modelled with smooth vector fields, i.e. differentiable in all regions where the system is defined, and where the solution trajectories are smooth. However, for real systems this assumption is not always valid, and in many examples the vector field can change suddenly, for example a ball bouncing against a visco-elastic support. If this type of system is applicable then the system can no longer be considered smooth, and is referred to as nonsmooth. In many situations the nonlinear system can be described by a set of functions that apply in separate regions of the phase space. This type of system is referred to as *Piecewise Smooth* (PWS) systems or *hybrid* systems as the equations defining the system are smooth for all values in the permitted n-dimensional phase space except for across the (n-1)-dimensional manifold that separates the regions. A PWS system with state x at time t can be written as

$$\dot{x} = f_i(x,t), \quad x \in S_i,$$

where f_i is defined in S_i and is smooth. PWS systems are often classified into three different categories (see [15]), namely

1. **Piecewise smooth continuous systems**: There is a discontinuity surface where the vector fields are equal but the derivative of the vector field across the surface is discontinuous.
2. **Filippov systems**: The vector field at the discontinuity surface is discontinuous.
3. **Impacting systems**: The discontinuity surface acts as a boundary between allowed and forbidden regions the of phase space. There will be a jump in the state at this boundary.

The system studied in this paper can be classified as both type-1 and type-3. The impacting of valves against their seat leads to type-3 discontinuities while the opening of the valves can be considered a smooth transition and so is of type-1.

In nonsmooth systems there can be a transition in the overall dynamics without the systems undergoing a standard bifurcation. This is for instance the case with a *grazing bifurcation*. A grazing bifurcation of a limit cycle occurs when the orbit approaches a discontinuity surface tangentially. The analysis of grazing bifurcations has attracted a lot of attention in recent years (see [2, 5, 6, 9, 12, 19, 20, 21, 30, 31]) and continuous to be a hot topic.

This paper will use numerical techniques to continue both stable and unstable periodic solutions of a nonsmooth system (see e.g. [1]). The method takes into account the jumps in state or change in vector fields at the discontinuity surfaces and determines the stability of limit cycles. The existence of periodic solutions created at a grazing point will also be investigated using the methods described in section 4.2. To the knowledge of the authors this is the first time these techniques have been applied to a system similar to the one analysed here.

The reminder of the paper will be split as follows. Section 2 will describe the damper model and the full dynamical system that will be studied. The next section, section 3, will describe the results of a set of simulations that give us a crude understanding of the types of dynamics that occur in the system for the given range of parameter values. A *stroboscopic* approach will be used with a constant initial

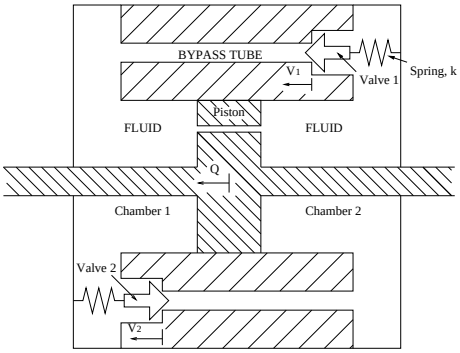

FIG. 2.1. *A schematic view of the hydraulic damper with relief valves*

condition. Section 4 uses a method to numerically follow the periodic orbits found in section 4. The different bifurcations that occur will be highlighted and the nonsmooth bifurcations will be analysed. Finally, section 5 makes some concluding remarks about the significance of this work.

2. Modelling. A number of authors have modelled the dynamical properties of hydraulic piston dampers [24, 26] of the kind used in many mechanical situations. Previous models for such dampers have typically studied the open loop dynamics and have shown that the fluid compressibility and head loss due to the orifice geometry and blow-off valves can have significant effects [10, 11, 14, 27]. The specific damper configuration studied in this paper is depicted in Figure 2.1, where the fluid fills the unshaded regions in both chambers 1 and 2. Under low piston velocity conditions the damper operates as a normal orifice damper. All the flow between chambers passes through the cylindrical orifice, of diameter d, which generates the pressure difference across the piston and hence a force. When the pressure difference becomes large enough, one of the *relief* (or *blow-off*) valves will open, which limits the force generated at high velocities. The critical pressure when this occurs is denoted by P_{crit}. The force response of the damper for an increasing velocity will then become piecewise as illustrated in Figure 2.2. In earlier work [11], we produced a parametric model of this damper incorporating the dynamics of the blow-off valves and the compressibility of the fluid. A good match was found with experimental data for the open loop dynamics.

This paper will consider simulations of this damper model embedded within the simple closed-loop system illustrated in Figure 2.3. There is a lumped body connected to a stationary wall via a linear spring and the damper is connected to the mass and the wall, in parallel to the spring. Hence, the general equation of motion for the system is given by

$$M\frac{d^2Q(t)}{dt^2} + KQ(t) + F_d(t) = F(t) \tag{2.1}$$

where $Q(t)$ is the displacement of the body with mass M, K is the linear spring stiffness, $F_d(t)$ is the force provided by the damper and $F(t)$ the external forcing. By letting

$$F(t) = \sigma \sin(\omega t), \tag{2.2}$$

where σ and ω is the amplitude and frequency of the external forcing, respectively,

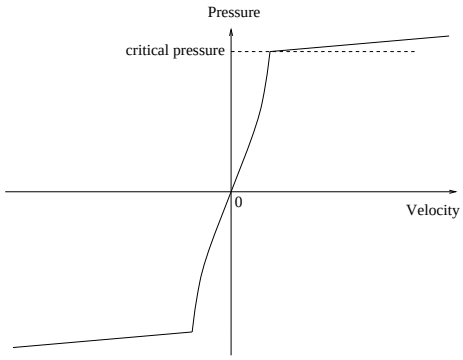

FIG. 2.2. *A sketch of the damper's pressure-velocity characteristic.*

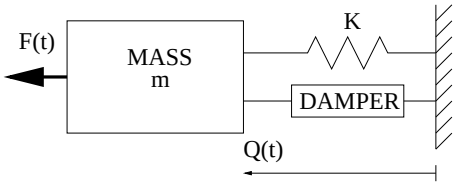

FIG. 2.3. *Diagram of the closed system used with a linear spring, stiffness K.*

and

$$F_d(t) = A\Delta P(t), \tag{2.3}$$

where A is the area of the piston, $\Delta P(t)$ is the pressure difference between the two chambers, and assuming the inertia of the piston is negligible the overall equation of motion for the closed-loop system can be written

$$M\frac{d^2Q(t)}{dt^2} + KQ(t) + A\Delta P(t) = \sigma\sin(\omega t). \tag{2.4}$$

2.1. The damper model. The system has three degrees of freedom, the displacement of the lumped mass, $Q(t)$, and the displacement of the two valves, $V_1(t)$ and $V_2(t)$. The pressure difference between the two chambers in Figure 2.1, $\Delta P(t)$, is calculated using the model of the damper developed in [11]. As $V_i(t^-) = 0$, for $i = 1, 2$, i.e. when one of the valves impact the valve seat, the impact law

$$\frac{dV_i(t^+)}{dt} = -r\frac{dV_i(t^-)}{dt} \tag{2.5}$$

is applied, where r is the *coefficient of restitution*, t^+ is the time immediately after impact and t^- the time immediately before. In this paper r is set to zero. The exact value of r is unknown for the damper modelled because the valve is unaccessible and so cannot be tested. A value of zero is a good approximation of the system and occurs in numerous examples where the energy wave produced by the impact does not rebound and so does not cause the impacting body to move away from the impacting surface. A common example of the sticking of the impacting object occurs in church bells [4], where the energy is dissipated as sound. Another situation where there is sticking is found in systems where the energy does not rebound due to the

geometry of the system rather than because of energy conversion such as an infinitely long Newton's Cradle. In our case energy can be dissipated through the viscous fluid analogous with a plug in a bath. Setting the coefficient of restitution to zero implies there will be no rebound of the valve as a result of the impact velocity. The valve can open immediately after closing if the pressure difference between the two chambers is sufficiently high as discussed above.

The dynamics of the relief valves and the pressure difference can be described by the following second order system derived in [11]

$$\frac{d^2V_1}{dt^2} = \begin{cases} (A_{v1}\Delta P(t) - \delta_1\frac{dV_1}{dt} - k_1(V_1(t)+V_{c1}))/m_{v1}, & \text{if } V_1 < 0, \\ (A_{v1}\Delta P(t) - k_1V_{c1})/m_{v1}, & \text{if } V_1 = 0 \text{ and } (A_{v1}\Delta P(t) - k_1V_{c1})/m_{v1} < 0, \\ 0, & \text{otherwise,} \end{cases} \tag{2.6}$$

$$\frac{d^2V_2}{dt^2} = \begin{cases} (A_{v2}\Delta P(t) - \delta_2\frac{dV_2}{dt} - k_2(V_2(t)+V_{c2}))/m_{v2}, & \text{if } V_2 > 0, \\ (A_{v2}\Delta P(t) - k_2V_{c2})/m_{v2}, & \text{if } V_2 = 0 \text{ and } (A_{v2}\Delta P(t) - k_2V_{c2})/m_{v2} > 0, \\ 0, & \text{otherwise,} \end{cases} \tag{2.7}$$

$$\frac{d\Delta P}{dt} = \frac{1+\zeta}{\zeta\beta\overline{V}}\left[A\frac{dQ}{dt} - \text{sign}(\Delta P(t))\left(\frac{-D_1+\sqrt{D_1^2+4D_2|\Delta P(t)|}}{2D_2} + R(V_1,V_2,t)\sqrt{|\Delta P(t)|}\right)\right], \tag{2.8}$$

where

$$R(V_1,V_2,t) = C_{po}\left(\frac{\gamma(\Xi_1+\Xi_2)^2}{1+\gamma(\Xi_1+\Xi_2)}\right)\pi d_v \sin(\alpha)\sqrt{\frac{2}{\rho}}, \tag{2.9}$$

and

$$\Xi_1 = \begin{cases} -V_1, & \text{if } V_1 < 0, \\ 0, & \text{otherwise,} \end{cases} \qquad \Xi_2 = \begin{cases} V_2, & \text{if } V_2 > 0, \\ 0, & \text{otherwise.} \end{cases} \tag{2.10}$$

The physical constant A_v is the area of the valve of diameter d_v, ζ is the proportional volume of chamber 1 compared to chamber 2, β is the compressibility constant of the fluid in the damper and $\overline{V}$ is the average volume of chamber 1. Taking right to left as the positive displacement direction in Figures 2.1 and 2.3, valve 1 will be open when the displacement V_1 is less than zero, see (2.10). Similarly a positive displacement of valve 2, $V_2 > 0$, indicates it is open. The losses due to a given valve deflection are characterised by an initial slope proportional to γ and maximum loss for the valve fully open of C_{po}. The equation motion for valve i is defined by the mass of the valve m_{vi}, spring stiffness k_i and damping term δ_i.

R is a measure of the magnitude of flow going through the valve and is strictly positive for values of valve half angle $\alpha < \frac{\pi}{2}$. The direction of flow is considered in (2.8) through the term $\text{sign}(\Delta P(t))$. The constants D_1 and D_2 represent the linear and quadratic head losses due to the fluid flow through the orifice and are given by

$$D_1 = \frac{128l\eta}{\pi d^4} \text{ and } D_2 = \frac{8c\rho}{\pi^2 d^4}, \tag{2.11}$$

where the orifice in the piston has length l and diameter d (cf. Figure 2.1). Further, η is the dynamic viscosity, ρ is the density of the hydraulic fluid, c is the discharge

coefficient of the piston orifice, and V_{c_i} is the precompression of the springs in relief valve i given by

$$V_{c_i} = \frac{P_{crit_i} A_v}{k}, \quad i = 1, 2. \tag{2.12}$$

The spring precompression determines the critical pressure assuming the area of the valve does not change.

Equation (2.6) represents relief valve 1. It includes terms for the spring of stiffness k_1, damping δ_1 and the forcing by the pressure difference between the two chambers acting on the area of the valve A_{v1}. The losses in the bypass tube are assumed to be small compared to the losses due to the piston orifice and valves. Equation (2.7) corresponds to (2.6) but for valve 2. The final equation (2.8) relates the compressibility of the fluid to the flows in the damper. For incompressible flow the volume flow, $A\frac{dQ}{dt}$, for a given piston velocity will flow in some proportion through the main orifice and bypass tubes. A compressible flow implies that there will be a difference between the theoretical flux ($A\frac{dQ}{dt}$) and the actual total flux of the orifice and bypass tubes. This difference is proportional to the rate of change of ΔP as seen in (2.8). The constant of proportionality is a function of the compressibility and average volume of the chambers, $\overline{V}$. If either the compressibility or volume of the chambers were decreased, there would be a larger rate of change of pressure difference for a given change in piston velocity. The damper would therefore become more responsive to rapid changes in the systems velocity.

2.2. Nondimensionalisation and parameters. In practice, the damper is likely to be designed to be as symmetric as possible, so the two valves are considered to be identical with the same spring stiffness, and the displacements of the valves are in the same direction as the piston. In all numerical results presented below, the positive displacements are for valve 2 and negative displacements are for valve 1.

Assuming the chambers are of equal volume so $\zeta = 1$ and we have symmetric springs so $A_{v1} = A_{v2}$, $\delta_1 = \delta_2$, $k_1 = k_2$ and $m_{v1} = m_{v2}$ we can reduce the number of coefficients appearing in the equations of the system (2.4)-(2.8). By letting

$$\begin{array}{llll} X_1 = V_1, & X_3 = V_2, & Q_1 = Q, & p = \frac{\Delta P}{P_{crit}} \\ X_2 = \frac{dV_1}{dt}, & X_4 = \frac{dV_2}{dt}, & Q_2 = \frac{dQ}{dt}, & \end{array} \tag{2.13}$$

and writing Equations (2.4)-(2.8) as a system of first order ordinary differential equations we get

$$\begin{aligned}
\frac{dQ_1}{dt} &= Q_2, \\
\frac{dQ_2}{dt} &= C_1 \sin(\omega t) - C_2 Q_1 - C_3 p, \\
\frac{dX_1}{dt} &= X_2, \\
\frac{dX_2}{dt} &= \begin{cases} C_4 p - C_5 X_2 - C_6 X_1 - C_7, & \text{if } X_1 < 0, \\ C_4 p - C_7, & \text{if } X_1 = 0 \text{ and } C_4 p - C_7 < 0, \\ 0, & \text{otherwise}, \end{cases} \\
\frac{dX_3}{dt} &= X_3, \\
\frac{dX_4}{dt} &= \begin{cases} C_4 p - C_5 X_4 - C_6 X_3 + C_7, & \text{if } X_3 > 0, \\ C_4 p + C_7, & \text{if } X_3 = 0 \text{ and } C_4 p + C_7 > 0, \\ 0, & \text{otherwise}, \end{cases}
\end{aligned}$$

TABLE 2.1
Parameter values used for simulations

Parameter	Old parameter	Value
C_1	$\frac{\sigma}{M}$	4×10^4
C_2	$\frac{K}{M}$	4×10^6
C_3	$\frac{AP_{crit}}{M}$	2×10^2
C_4	$\frac{A_v P_{crit}}{m_v}$	1.98×10^4
C_5	$\frac{\delta}{m_v}$	5×10^3
C_6	$\frac{k}{m_v}$	2×10^7
C_7	$\frac{V_c}{m_v}$	1.96×10^4
C_8	$\frac{(1+\zeta)A}{\zeta\beta\overline{V}P_{crit}}$	4.21×10^5
C_9	$-\frac{(1+\zeta)D_1}{\zeta\beta\overline{V}P_{crit}2D_2}$	-1.66×10^4
C_{10}	$\frac{(1+\zeta)^2\sqrt{P_{crit}}}{(\zeta\beta\overline{V}P_{crit})^2 D_2}$	2.89×10^3
C_{11}	$\frac{(1+\zeta)C_{po}\gamma\pi d_v \sin(\alpha)\sqrt{2}}{\zeta\beta\overline{V}\sqrt{P_{crit}}\sqrt{\rho}}$	1.31×10^{14}
C_{12}	γ	4×10^5
r		0

$$\frac{dp}{dt} = \Big\{ \; C_8 Q_2 - \text{sign}(p) \left(C_9 + \sqrt{C_9^2 + C_{10}|p|} + R(X_1, X_3, t)\sqrt{|p|} \right), \tag{2.14}$$

where

$$R(X_1, X_3, t) = C_{11} \left(\frac{(-X_1\mathcal{H}(-X_1) + X_2\mathcal{H}(X_2))^2}{1 + C_{12}(-X_1\mathcal{H}(-X_1) + X_2\mathcal{H}(X_2))} \right) \tag{2.15}$$

and $\mathcal{H}$ is the Heaviside step function, the constants $C_1 - C_{12}$ are defined in Table 2.1 and the impact law (2.5) is used for the valve-valve seat impact. The values used are not taken from a particular physical system but are indicative of a typical macro-scale device and are used here to illustrate the type of dynamics that can occur. The forcing frequency ω will be the parameter that is varied to capture the different dynamics.

3. Simulation results. The dynamics of the closed-loop system presented in this paper can be categorised by three main frequency regions. Firstly at low forcing frequencies the damper is responsive enough to ensure there is only one valve open at any moment. The second region to be considered is for very high frequencies where the compressibility of the fluid becomes the overriding factor. In this region the system becomes sluggish and a point is reached when the critical pressure will not be reached, and the valves will never open. In between these two regions there is a possibility of both valves being open at the same time. The dynamics in this intermediate frequency range form the main focus of this paper. First though, let us consider the dynamics of low and high forcing frequencies.

3.1. Low and high frequency forcing; regular motion. At relatively low forcing frequencies the system behaves in a regular period-one manner (i.e. repetitive motion in which each valve opens once per period). The motion of the mass is sinusoidal and each valve has time to open and close before the other opens as shown in Figure 3.1. There are oscillations of the valve, however these oscillations do not affect the motion of the mass since the force generated by the damper is smaller than the overriding force generated by the linear spring in Figure 2.3. The forcing

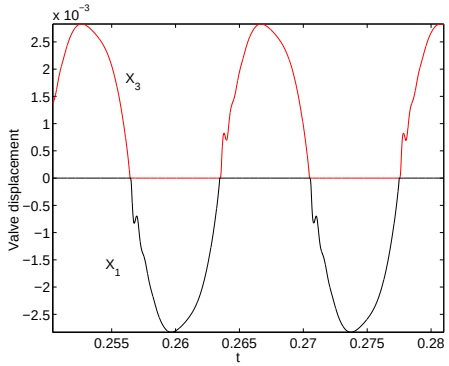

(a) Displacement of valves versus time

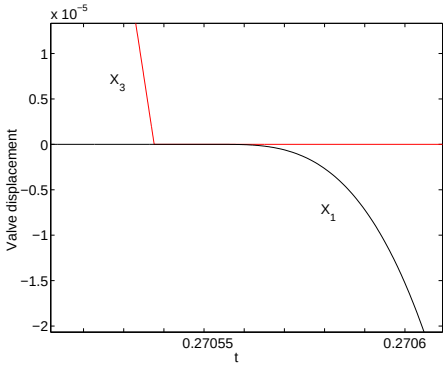

(b) Magnified section of Figure 3.1(a) showing valve releasing from the valve seat.

FIG. 3.1. *Low frequency motion, $\omega = 447 rad/s$. Displacement of the valves versus time. The red line corresponds to valve 2 (Q_3) and the black line to valve 1 (Q_1).*

frequency used in Figure 3.1 is 10% of the natural frequency of the spring valves which is 4.47×10^3 for the parameter values in Table 2.1. The response of the mass is more or less purely sinusoidal with the same frequency as the forcing frequency.

At high frequencies numerics show that the dynamics are once again regular and dominated by the compressibility of the fluid inside the main chambers of the damper. The pressure difference inside the damper does not get high enough to open the valves before the direction of the mass is reversed. A result of the sponginess of the fluid is that the motion from the mass is absorbed before the valves can open. The damper then only operates in the low pressure region with the valves closed. This increased effect of the compressibility means the force generated effectively becomes a linear function of the mass displacement rather than a nonlinear function of the velocity. Overall, the combined effect of these two factors leads to a linear force from the damper. The whole system is then linear so there will be no irregular dynamics occurring in this high frequency region. Figure 3.2 shows a time history of the mass displacement, at a forcing frequency one thousand times the natural frequency of the relief valves. It can clearly be seen in Figure 3.2 that the system decays to low amplitude oscillations rather than producing a high amplitude periodic motion as it did at the lower frequency forcing. The frequency of the local low amplitude oscillations is again the same as the forcing frequency.

3.2. Mid-frequency forcing; chaotic motion. More unpredictable dynamics occurs when the forcing frequency is in an intermediate range between the two cases described above. We consider in particular ω in the range $6500 - 20000$ which is between about 1.5 and 4.5 times the natural frequency of the spring valves. One of the easiest ways to visualise the change in dynamics of a system is to introduce a Poincaré section Σ and plot a point every time the trajectory crosses the section as the forcing frequency changes. This can be seen in Figure 3.3 as a stroboscopic plot, where the last 25 cycles, of a run of 500 cycles, are plotted. Thus the results present the steady state dynamics after the transients have died out. The Poincaré section Σ is taken at $Q_2 = 0$ so the section is defined as

$$\Sigma := \left\{ (Q_1, Q_2, X_1, X_2, X_3, X_4, p) \in \mathbb{R}^7 \mid Q_2 = 0 \right\}. \tag{3.1}$$

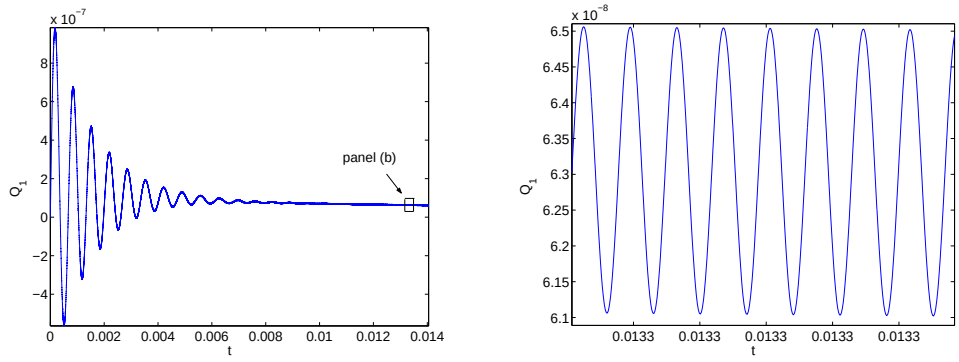

(a) Displacement of mass versus time. (b) Magnified section of Figure 3.2(a).

FIG. 3.2. *High frequency motion, $\omega = 4.47 \times 10^6 rad/s$. Displacement of mass versus time.*

The corresponding bifurcation diagram plots the mass displacement Q_1 for each intersection with the Poincaré section. All simulations in this section have initial conditions $Q_i(0) = 0$ for $i = 1, 2$, $X_j(0) = 0$ for $j = 1, \ldots, 4$ and $p(0) = 0$. The model was simulated in Matlab [16] with great care taken using hit crossing detection to ensure the valve opening and closing events were computed accurately. Hence each simulation took on average half an hour to compute on a Pentium 3 processor with clock speed 1 GHz, running Microsoft Windows NT. The number of points available in a realistic time period is therefore limited. The aim of this 'brute force' bifurcation diagram in Figure 3.3 is to find the broad features of the system so that interesting regions of parameter space can be investigated further with more sophisticated methods.

Figures 3.4 and 3.7 are similar bifurcation diagrams for a smaller forcing frequency range. In both figures a naïve path-following scheme has been used to capture the trend in the dynamics. The initial conditions for each new frequency value was chosen to be the final state of the previous simulation in an attempt to remain on the same attractor. Figure 3.7 shows a large amount of 'noise' on top of the periodic solutions. In the frequency range shown in the figure there is a coexisting chaotic attractor. The basins of attraction for the 7-degree-of-freedom system in this region seems not to be as regular as for lower frequencies and as a result the simulations can jump between solutions.

The remainder of this section will look at the different dynamics displayed by the system. In Figure 3.3 the different regions are labelled A-D, which we will refer to in some of the figures in this section.

For frequencies below 7.18×10^3 rad/s the system behaves symmetrically as seen in Figure 3.5(a). The only stable motion found below this frequency are period-one orbits, illustrated in Figure 3.4. In Figure 3.5(a) one can see that both valves are alternately open by the same amount, which leads to a symmetric force and a symmetric mass motion about zero displacement. The motion of the valves in Figure 3.5(a) are different from those in Figure 3.1(a) since there are time intervals where both valves are open at the same time. Nevertheless the motion is still period-one and symmetric. Furthermore, the motion of the valves shown in Figure 3.5(a) displays a typical event sequence for frequencies that lead to period-one motion.

When the forcing frequency reaches 7.18×10^3 rad/s the system undergoes a symmetry breaking bifurcation (a super-critical pitchfork bifurcation). At this type

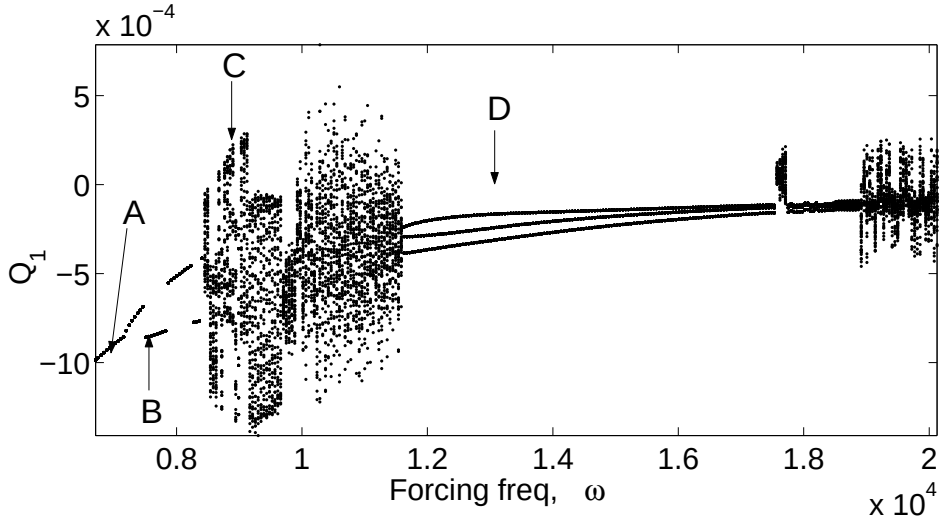

FIG. 3.3. *Bifurcation diagram showing mass displacement versus forcing frequency at the Poincaré section* $Q_2 = 0$. *The amplitude of forcing is* $2 \times 10^6 N$.

of bifurcation a stable symmetric period-one branch turns unstable and two stable asymmetric period-one solutions are born. The new stable branches coexist up to 8405 rad/s, shown in Figure 3.4 as the two lines separating from one another. The blue solution will be referred to as the *top* solution while the red branch is part of the *bottom* attractor. Figures 3.5(c) and 3.5(b) illustrate the two stable solutions at 8000 rad/s. For the bottom attractor (the higher magnitude of mass displacement in Figure 3.4) in Figure 3.5(b) the valves are open an unequal amount. Valve 1 (negative displacement) opens much more compared to valve 2. This is in direct contrast to Figure 3.5(c) where valve 2 opens more than valve 1. The motion of the valves for the two attractors are mirror images of each other. This difference in motion of the two valves is caused by the change in the force trajectory of the damper. The damper in the bottom attractor produces a much larger positive force than for the top attractor.

For increasing frequencies the asymmetric period-one solution suddenly disappears and a nonperiodic (chaotic) solution appears. This occurs at the point when one of the valves encounters a low-velocity impact on the valve seat during the transient stages of the simulations. The previously impacting trajectory no longer impacts the valve seat, which leads to a quantitatively different trajectory which lies within the basin of attraction of a coexisting attractor. The possibility of jumps to coexisting nonperiodic attractors can often be encountered in nonsmooth systems. Here a forcing frequency of 8406.4 rad/s leads to motion where valve 1 impacts the valve seat whereas a slight increase (0.1 rad/s) of the forcing frequency leads to the valve completely missing the valve seat, which yields a completely different mass trajectory. In between these two forcing frequencies there will be a point when valve 1 impacts the valve seat with a zero velocity. This is defined as the grazing of valve 1 on the valve seat. The two chaotic attractors can be seen in Figure 3.4 as the red and blue dots.

After the nonperiodic solution (through section C in Figure 3.3) there is a large span of forcing frequencies that produce a stable period-three solution. A typical

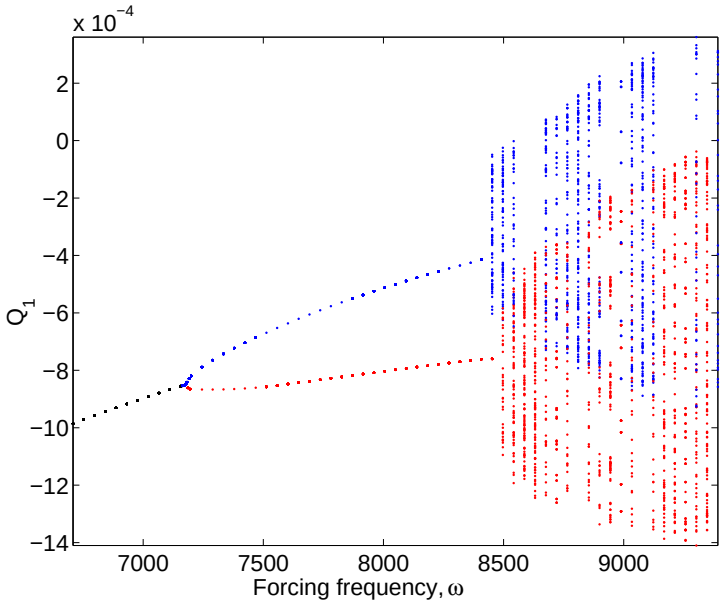

FIG. 3.4. *Bifurcation diagram for low forcing frequencies showing mass displacement versus forcing frequency with Poincaré section at* Σ. *Amplitude of forcing* $= 2 \times 10^6 N$.

phase portrait of the period-three orbit can be seen in Figure 3.6(a) for a forcing frequency of 13.86×10^3 rad/s.

In the case of the higher frequency route to chaos there is no sudden jump from periodic to nonperiodic. Instead there seems to be a period doubling cascade of the solution as the forcing frequency increases. Figure 3.7 illustrates the case of the period-three solution becoming a period-six solution at around 1.825×10^4 rad/s. The period-six solution can be seen in Figure 3.6(b) for a forcing frequency of 1.843×10^4 rad/s.

4. Examining the onset of chaos. For most applications the most important areas of parameter space to understand is where transitions between stable, unstable, and chaotic motions occur or where such motions cease to exist. This section will focus on forcing frequencies in the range 7000-19000 (see section 3.2 and Figure 3.3). The previous section did not carefully follow any of the solution branches and so we were unable to accurately detect the bifurcation points. In what follows we will follow solution branches by using a continuation algorithm to allow for both stable and unstable branches of periodic orbits to be continued through parameter space.

4.1. Numerical continuation. In the present paper we are generally interested in recurrent motion and in particular limit cycles. From this perspective, the main idea of the implemented continuation algorithm is to locate fixed points of Poincaré maps (which is equivalent to finding periodic orbits) and to follow branches of such solutions under parameter changes. To do this we introduce a Poincaré section in the phase space, such that transversal intersections of the section are assured and so that any other events (impacts or sticking) are relatively far away from the section. The method to continue fixed points of this map is an extension of that presented in [8] to take particular account of the various switching hyperplanes in the phase space of

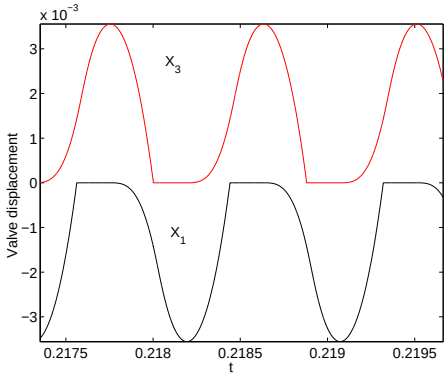

(a) $\omega = 7.15 \times 10^3$rad/s (near A in Figure 3.3).

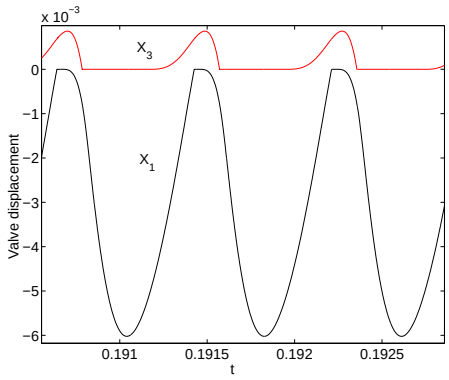

(b) $\omega = 8 \times 10^3$rad/s for top attractor (near B in Figure 3.3).

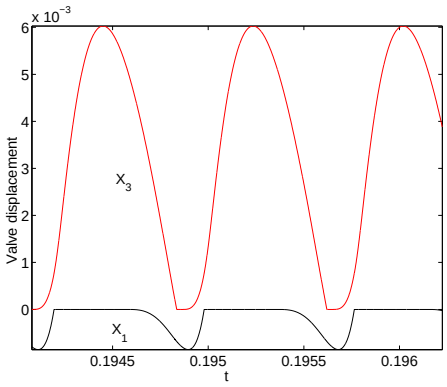

(c) $\omega = 8 \times 10^3$rad/s for bottom attractor (near B in Figure 3.3).

FIG. 3.5. *Displacement of the valves versus time for given forcing frequencies.*

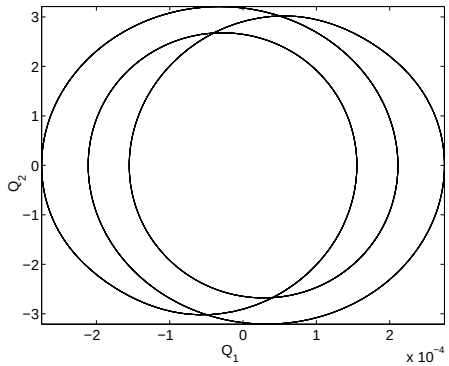

(a) $\omega = 13.86 \times 10^3$rad/s (near D in Figure 3.3) showing period-three motion.

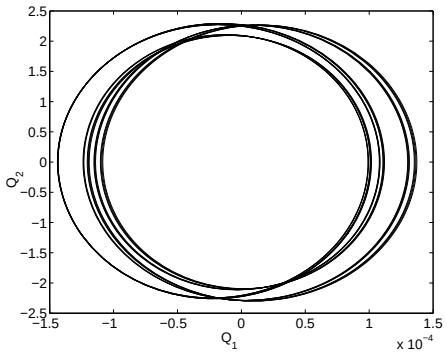

(b) $\omega = 18.43 \times 10^3$rad/s showing period-six motion.

FIG. 3.6. *Phase portraits showing mass displacement versus mass velocity.*

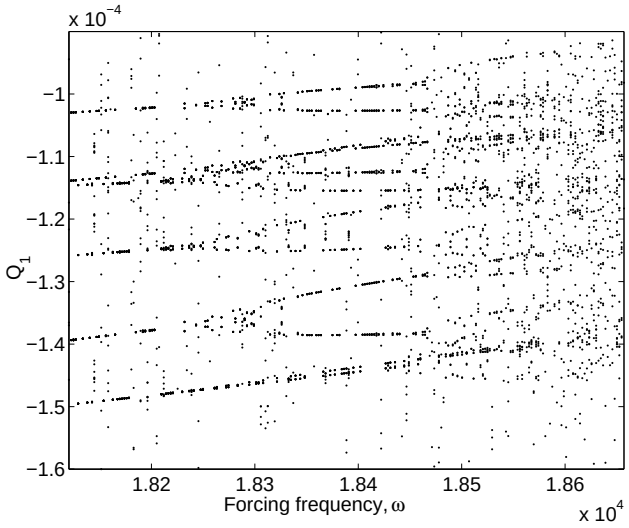

FIG. 3.7. *Bifurcation diagram for high forcing frequencies showing mass displacement versus forcing frequency with Poincaré section at* Σ. *Amplitude of forcing is* $2 \times 10^6 N$.

(2.14). The key idea is to locate fixed points using Newton's method. This requires the Jacobian of the Poincaré map, which is found by solving the first variational equations for the nonsmooth system. However it is not possible to solve the first variational equations in as straight forward way as you would for a smooth system since any perturbations caused by the discontinuities have to be taken into account. This is done by applying corrections to the flow Jacobian at the discontinuities. In practise this is achieved by multiplying the flow Jacobian with correction matrices (sometimes referred to as *saltation matrices*). These matrices are found by the use of local *discontinuity mappings* [8, 12, 15, 17]. Further, convergence of Newton's method is only assured if a periodic solutions is hyperbolic or if the trajectory does not approach any of the discontinuity surfaces tangentially (at, for instance, grazing). When a hyperbolic solution is found we know from the Implicit Function Theorem that there exists a branch of hyperbolic periodic solutions under any parameter change. Once a periodic orbit has been found, and a parameter has been changed, polynomial extrapolation is used to predict initial conditions for the new Newton iterations. Further details on how to implement and use this method in nonsmooth systems can be found in [1, 8, 22, 23].

The Jacobian of the Poincaré map can also be used to assess the linear stability of a solution located with the above mentioned method. The condition for stability being that all eigenvalues of the Jacobian are within the unit circle, but if any of the eigenvalues are outside the unit circle the solution is unstable.

As with smooth systems, the stability of periodic orbits of nonsmooth systems can be lost under parameter variation through standard bifurcations- saddle-node (fold), pitch-fork (symmetry breaking), flip (period doubling) or Hopf which can be detected from the spectrum of the Jacobian matrix. In addition, we find nonstandard bifurcations that are unique to nonsmooth systems [3]. Here we focus on one such possibility, the grazing bifurcation.

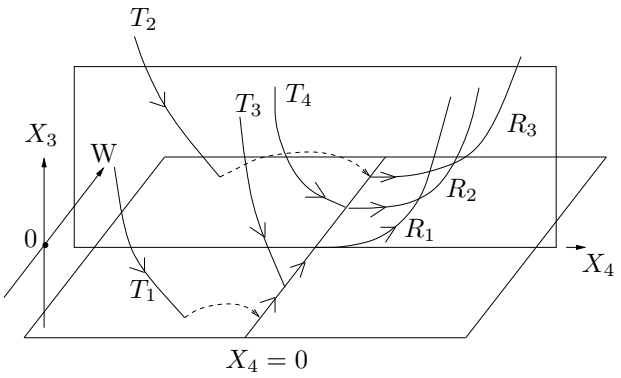

FIG. 4.1. *Sketch of the possible dynamics of valve 2 where* $W = \Delta P - C_7/C_4$ *from section 2.2,* X_3 *is the displacement of the valve,* X_4 *is the velocity of the valve.*

4.2. Grazing bifurcations. For the system modelled in this paper it is the motion of a valve that can cause a grazing bifurcation and thereby drastically change the dynamics. A grazing event occurs when a valve impacts a valve seat with zero velocity.

A schematic of the various ways in which a valve can impact the valve seat is depicted in Figure 4.1. For definiteness we suppose the second valve undergoes the grazing. Owing to the symmetry between the second and third set of equations in (2.14), similar considerations apply to the first valve. Trajectory T_1 represents the case where the valve impacts the valve seat and the pressure is below the critical opening pressure for the valve (as discussed in section 2). The velocity of the valve will be vanish ($X_4 = 0$) since the coefficient of restitution is assumed to be zero (see (2.5)). The valve will remain closed until the critical pressure is reached, i.e. when $W = 0$, whereafter it will leave the $X_3 = 0$ plane along R_1. T_3 is a special case of T_1 where the valve displacement X_3 approaches zero as the velocity X_4 approaches zero for a pressure less than the critical pressure. It is unlikely that this will occur however, since the force of the valve spring will be much greater than that of the pressure forcing it open. In the limit however there could be a grazing condition as the intersection of T_3 with X_4=0 approaches $W = 0$.

For impacts of the valve when the pressure in the system is greater than the critical pressure ($W > 0$) there will be an immediate rebound of the valve. In the general case the trajectory will follow a similar path to T_2 in Figure 4.1. The valve will impact on the valve seat with a negative velocity on to the X_3=0 plane. The velocity X_4 will jump to zero before rebounding along the trajectory R_3. If the intersection of T_2 with X_3=0 coincides with the line X_4=0 there is a grazing event since the displacement and velocity of the valve is instantaneously zero, illustrated by T_4. The trajectory of the valve will then follow R_2.

A grazing point on a bifurcation diagram can be defined as the point at which a previously non-impacting periodic orbit impacts a surface tangentially for a change in the bifurcation parameter. Alternatively a grazing point can be defined for a previously impacting orbit that stops impacting for a small change in the bifurcation parameter. In the generic case a grazing bifurcation can lead to both impacting and non-impacting solutions. To find which of these occurs, and to fully unfold the dynamics, the technique of discontinuous mappings [8] can be used. See Appendix A for an application of that technique to the damper modelled in this paper.

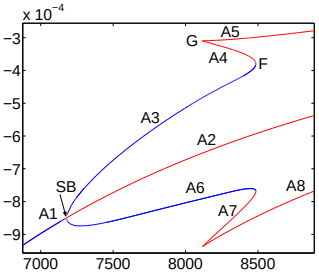

(a) Period-one symmetry breaking

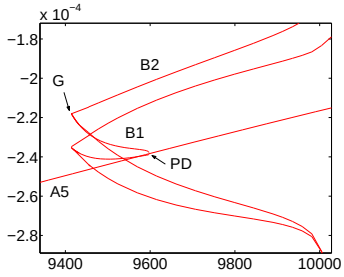

(b) Unstable period-doubling to grazing

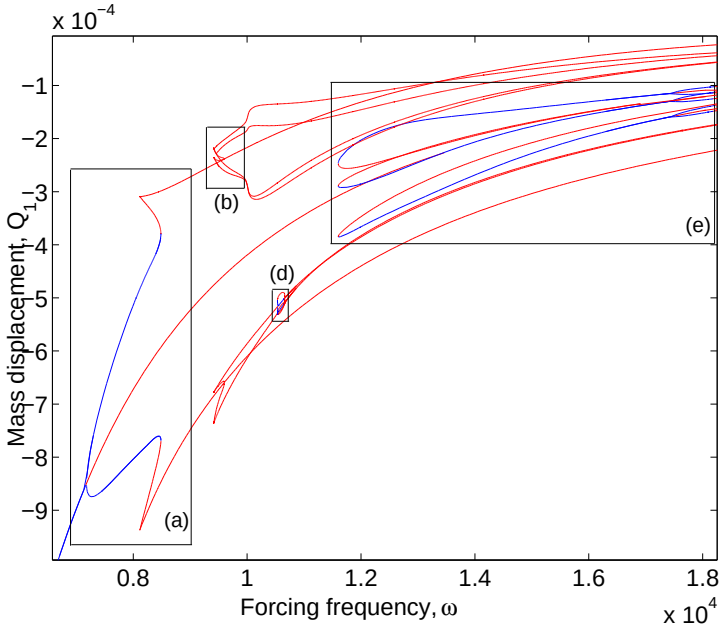

(c) Full bifurcation diagram

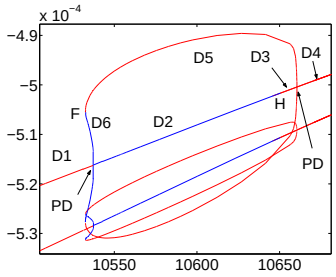

(d) Stable period-two period-doubling

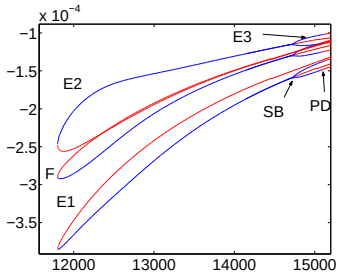

(e) Period-three stable solution

FIG. 4.2. *Bifurcation diagram for investigated forcing frequencies. Blue points = stable; Red points = unstable. Bifurcation points indicated as: SB for symmetry breaking; H for a Hopf; PD for period-doubling; F for a fold; and G for grazing.*

4.3. Numerical continuation results. A bifurcation diagram for the mid frequency region (6500-18000) is shown in Figure 4.2, where the path following technique described in section 4.1 is used. In what follows the Poincaré section used in the bifurcation diagrams is Σ, which is given in (3.1).

Up to $\omega = 7180$ the only solution found is a stable symmetric period-one orbit labelled as branch A1 in Figure 4.2(a). This solution branch undergoes a super-critical symmetry breaking (pitchfork) bifurcation at $\omega = 7180$ as one of the eigenvalues of the Jacobian of the Poincaré reaches the unit circle along the positive real axis. The resulting unstable branch A2 continues to exist for the whole parameter range above $\omega = 7180$. As expected, two new stable branches asymmetric period-one solutions are born at the pitchfork bifurcation, labelled A3 and A6 in Figure 4.2(a), where the trajectories corresponding to the stable branches are mirror images of each other, as discusses in section 3.2. These two branches exist up to 8485.8, where an eigenvalue of the Jacobian crosses the unit circle along the positive real axis indicating a fold bifurcation. It is notable that the stable branches (A3 and A6) seem to exist for a larger range of forcing frequencies than observed in section 3.2 in Figure 3.3, where a brute force stroboscopic approach was used. An explanation for this could be that one of the valves impacts with low-velocity before the transients have died out, which causes the solution to jump to a coexisting chaotic attractor (see also section 3.2) instead of the stable period-one solution. This indicates that the chaotic motion seen in Figure 3.3 is not created as a direct result of bifurcations of the period-one solutions branches A3 or A6. At $\omega = 8485.8$ two unstable branches A4 and A7 fold back as the forcing frequency decreases and finally cease to exist at 8116.1, i.e. they cannot be followed further. The reason is that valve 1 (or valve 2) stops impacting the valve seat at this point, i.e. the trajectory grazes the valve seat, indicating that a grazing bifurcation has been encountered (see further section 4.4 and Figure 4.3). As expected, the largest eigenvalue in magnitude of branches A4 and A7 tends to infinity as it approaches the grazing point. There are two other unstable solution branches, A5 and A8, that appear at $\omega = 8116.1$, where the branches A4 and A7 disappeared, that can be continued for increasing frequencies. The eigenvalues with the largest magnitude (actually a complex pair) of branch A5 at the grazing point is 1.09. In contrast to the the branches A4 and A7, trajectories corresponding to branches A5 and A8 have non-impacting trajectories of one of the valves for forcing frequencies above $\omega = 8116.1$, and at 8116.1 the non-impacting valve just grazes the seat (see Figure 4.3). The two cases are mirror images with valve 1 grazing on branch A5 (cf. in Figure 4.3(a)) and valve 2 grazing on branch A8 (cf. Figure 4.3(b)). This particular situation will be discussed further in section 4.4.

The branches A5 and A8 can now be continued for increasing frequencies. At $\omega = 9598$ the solution branch undergoes a subcritical flip (period-doubling) bifurcation as one of the eigenvalues of the Jacobian becomes -1 at this frequency. The period-two branches B1 in Figure 4.2(b) exist for decreasing frequencies until they abruptly stop at approximately $\omega = 9414.4$ in another grazing bifurcation. This situation is similar to what happened to the period-one solution discussed above. Also, similar to the period-one case, there are a number of different solution branches coming together at this grazing point(see further section 4.4). In Figure 4.2(c) we can see an unstable period-two branch, D1 in Figure 4.2(d), and an unstable period-four branch, B2 in Figure 4.2(b). These branches are in addition to the period-two branches from the period-doubling bifurcation, being born at $\omega = 9414.4$ and can be continued for increasing frequency. The period-two branch D1 can be continued for the whole mid-

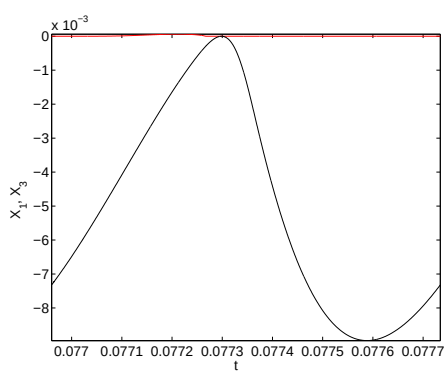

(a) Grazing of valve 1 for branch 'A5' in Figure 4.2(a)

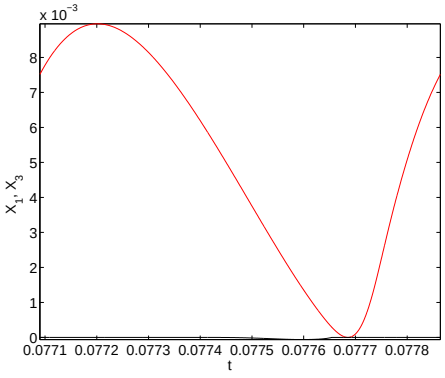

(b) Grazing of valve 2 for branch 'A8' in Figure 4.2(a)

FIG. 4.3. *Time histories showing grazing of the valves on the branches 'A5' and 'A8' in Figure 4.2(a).*

frequency interval, but at $\omega = 10538$ it undergoes a supercritical period-doubling bifurcation and turns stable along D2. The new stable period-four branches (see D6 in Figure 4.2(d)) exist for decreasing frequencies until $\omega = 10533$ where the solution undergoes a fold bifurcation as an eigenvalue crosses $+1$. The resulting unstable period-four branch D5 continues for increasing frequencies up to $\omega = 10660$ where it connects back to the original period-two branch at a period-doubling bifurcation. The stable period-two solution, D2, continues for increasing forcing frequency up to $\omega = 10651$ where two complex conjugate eigenvalues of the Jacobian leave the unit circle resulting in a Hopf bifurcation. The period-two branch continues as the unstable branch D3 up to the period-doubling bifurcation, where it comes together with the branch D5 after which point the unstable period-two branch D4 continues for all the investigated frequency range.

For higher forcing frequencies there exists a stable and an unstable symmetric period-three solution. The solutions are born at a fold at $\omega = 11600$ (see Figure 4.2(e)) in a similar way to the two stable period-one solution at low frequencies, producing a stable period-three, E2, and an unstable period-three, E1. The stable period-three solution exists with the unstable branch up to ω =17480 at which point there is a symmetry breaking bifurcation followed by a period-doubling cascade to chaos as suggested by Figure 3.7.

Let us now take a closer look at what happens at the different grazing bifurcations.

4.4. Analysis of grazing bifurcations. In the discussion in section 4.3 two different grazing bifurcations were encountered, at $\omega = 8116.1$ and $\omega = 9414.4$ (see Figure 4.2(c)), where period-one and period-two limit cycles experienced grazing, respectively. Let us take a closer look at the mechanism and behaviors in the vicinity of these grazing bifurcations and also compare what the conditions outlined in Appendix A predict and what the numerics discussed above show. The section Π used for the grazing bifurcation analysis is taken at the grazing point of the grazing valve, defined for valve 2 as

$$\Pi := \{(Q_1, Q_2, X_1, X_2, X_3, X_4, p) \mid X_4 = 0\}.$$

Let us start at the grazing of the period-one orbits at $\omega = 8116.1$. Here two

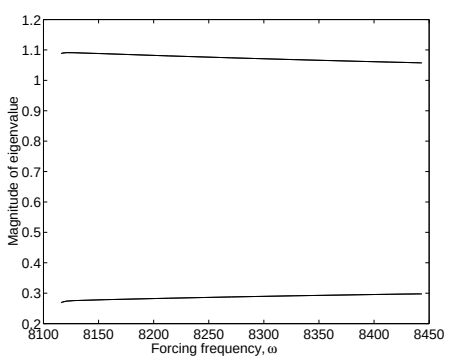

(a) Magnitude of eigenvalues of branch A5 in Figure 4.2(a)

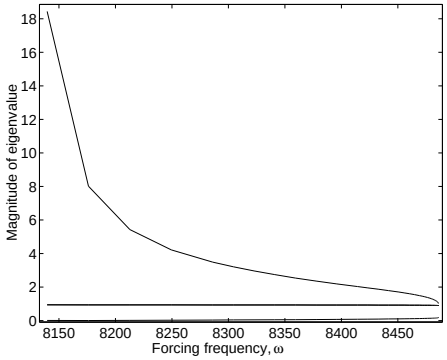

(b) Magnitude of eigenvalues of branch A4 in Figure 4.2(a)

FIG. 4.4. *Eigenvalues for branches A4 and A5 in Figure 4.2(a) up to the grazing point.*

unstable branches come together in phase and parameter space for all states but their eigenvalues are very different from each other. One one hand, branch A4 has one real eigenvalue larger than one in magnitude which increases exponentially in magnitude as the solution approaches the grazing point (see Figure 4.4(b)). On the other hand, branch A5 has two complex conjugate eigenvalues outside the unit circle that does not change much as the solution approaches the grazing (see Figure 4.4(a)). Both these scenarios fit perfectly in to what is to be expected in a grazing system. In the former case the nonzero elements of the saltation matrix that is involved in the grazing bifurcation tends to infinity as the grazing bifurcation is approached, thus the large magnitude of the eigenvalue. In the latter case the trajectory does not know that it will soon graze one of the surfaces, which was the case in the former situation, and thus the eigenvalues do not change more than they would have away from the grazing bifurcation.

In the case of the period-one grazing point at 8116.1 the only impacting solution we found numerically is the period-one solution with only a single impact per period as plotted in Figure 4.2. It is notable that the direction of the impacting period-one orbit and the non-impacting period-one orbit both exist on the same side of the bifurcation point.

The observations from the numerics can be verified by using the analysis outlined in Appendix A. The existence conditions for the orbits generated at the grazing point are derived in Appendix A along with the direction of the solution branches as they leave the grazing point. The system and existence conditions are listed as (A.21)-(A.23). The impacting surface, $h(x,\mu)$, is defined as the impacting of valve 2 (as is the case with the period-two/four grazing seen in Figure 4.2(b)) so $(D_\mu h)(0,0) = 0$, $(D_x h)(0,0) = X_3$ from (2.14). The directions of the impacting branches are defined by the argument at the end of Appendix A.

When applying the grazing analysis to the period-one grazing point we obtain the following matrices with reference to Appendix A.

$$A = \begin{bmatrix} 0.0467 & 4.4042\times10^{-4} & 0.3208 & 8.889\times10^{-6} & 0.0015 & -9.315\times10^{-8} & -0.0155 \\ -1861 & 0.0931 & -377.25 & -0.0059 & -76.58 & -0.0124 & 8.807 \\ -0.9529 & 3.677\times10^{-4} & -1.2709 & -2.180\times10^{-5} & -0.0155 & 1.558\times10^{-5} & 0.0220 \\ -7050 & -11.6379 & 56164 & 0.9760 & 7897 & 1.1580 & -1233 \\ 0 & 0 & 0 & 0 & 0 & 0 & 0 \\ 0 & 0 & 0 & 0 & 0 & 0 & 0 \\ 0.6160 & -0.0027 & 11.15 & 1.95\times10^{-4} & 1.2554 & 1.27\times10^{-4} & -0.2081 \end{bmatrix}$$

$$B = \begin{bmatrix} 0 & 0 & 1278.1 & 0 & 0 & 0 & 0 \end{bmatrix}^T$$

$$C = \begin{bmatrix} 0 & 0 & 1 & 0 & 0 & 0 & 0 \end{bmatrix}$$

$$M = \begin{bmatrix} 39392 & 5.3954 \times 10^7 & 36804 & 1.4788 \times 10^8 & 0 & 0 & -56776 \end{bmatrix}^T$$

Using these values we find that the only possible impacting orbit is the observed period-one orbit on the same side of the bifurcation as the non-impacting orbit. It should be noted that while the stability of the orbits cannot easily be calculated for this seven-dimensional system, the impacting orbits are almost certainly going to be unstable because the magnitude of one of the eigenvalues will tend to infinity as the orbit approaches the grazing point.

At the grazing point at $\omega = 9414.4$ the numerics suggest more than two periodic orbits are created. A suggestion of the possible dynamics can be obtained from Figure 4.2. Two non-impacting period-two solutions are found at the period-doubling bifurcation. These orbits annihilate at the grazing point where a period-four single-impacting solution is produced toward the top of Figure 4.2 and in Figure 4.2(b). A period-two single-impacting solution is born toward the bottom of Figure 4.2 at $\omega = 9414.4$. All the impacting orbits found using the numerics occur on the same side of the grazing point as the non-impacting orbit. The impacting orbit solution branches from a grazing point are in general unstable as the magnitude of the eigenvalue of the solution tends to infinity as seen in Figure 4.4(b). As such there is a possibility of many unstable solutions being produced at the grazing point that cannot easily be found using simple numeric searches.

The system in (A.21) should be solved exactly at the grazing point. The values taken for the following calculations are taken from the non-impacting period-two orbit computed at the grazing point.

$$A = \begin{bmatrix} -0.8360 & 2.4027 \times 10^{-4} & 0.0456 & 2.5376 \times 10^{-6} & -0.0160 & -1.0459 \times 10^{-7} & -0.0059 \\ -771.3872 & -0.7168 & -438.1495 & -0.0138 & 70.3298 & 4.9400 \times 10^{-4} & 18.8140 \\ -1.3322 & -0.0011 & 1.6014 & 3.4050 \times 10^{-5} & -0.0324 & -4.7202 \times 10^{-7} & 0.0389 \\ -5551.8 & 2.0496 & -24675 & -0.6015 & 1264.2 & 0.0118 & -225.9256 \\ -1.2104 & -7.9632 \times 10^{-4} & 0.8271 & 1.5791 \times 10^{-5} & -0.0182 & -2.5528 \times 10^{-7} & 0.0199 \\ -6314.3 & 0.1876 & -18797 & -0.4705 & 952.8446 & 0.0089 & -174.0410 \\ -0.6232 & 6.4932 \times 10^{-4} & -4.5000 & -1.1041 \times 10^{-4} & 0.1869 & 1.8835 \times 10^{-6} & -0.0613 \end{bmatrix}$$

$$B = \begin{bmatrix} 0 & 0 & 0 & 1031 & 0 & 0 & 0 \end{bmatrix}^T$$

$$C = \begin{bmatrix} 0 & 0 & 1 & 0 & 0 & 0 & 0 \end{bmatrix}$$

$$M = \begin{bmatrix} 60182 & 1.8030 \times 10^6 & 29718 & 1.8656 \times 10^8 & 32028 & 1.7653 \times 10^8 & 21317 \end{bmatrix}^T$$

Using these values, e from (A.17) produces $e = -1.6132 \times 10^4 < 0$. The non-impacting orbit will therefore exist for the bifurcation parameter $\mu < 0$. The quantity $s(n)$, for a period-n impacting orbit, can be calculated from (A.24). The resulting computation produces a value less than zero for all single impact periodic orbits denoted as impact sequence (n) for $n = 1, \ldots, 50$, which was the limit of the computers

matrix inversion using Matlab [16]. Since $s(n) < 0$ and $e < 0$, μ must also be negative if conditions (A.22), (A.23) and (A.25) hold (are positive). The conditions do hold for all the single-impact orbits up to period-fifty indicating that there can be at least fifty different unstable impacting orbits being generated at the grazing point in the same direction as the non-impacting orbit.

The analysis can be extended to more complex impacting sequences although it is not required here because we have already shown that a huge number of unstable orbits are generated at the grazing bifurcation. It seems natural therefore to suppose that this family of unstable periodic orbits is in fact infinite in number and forms part of the backbone of the numerically observed non-periodic attractor. However, it is also possible that the first grazing could create a chaotic invariant set. The set could become stable at the the fold of the other attractor at $\omega = 8486$ (boundary crisis event) when the chaotic attractor would dominate the dynamics. At the second grazing point the chaotic attractor changes type as the unstable orbits are born.

4.5. Quasi-periodic motion and chaos. In section 4.4 we showed that the source of the chaotic attractor could be the grazing bifurcation at $\omega = 9414.4$. The method used the properties of the grazing orbit to predict the orbits that will be created at the bifurcation. However, if we look more closely at the structure of the nonperiodic orbits we find that there may be another source of chaos.

A convenient way of investigating the nature of a nonperiodic solution is to create a delay plot of the dynamics in the Poincaré section Σ used to create Figure 3.3 (i.e. a Poincaré section at $Q_2 = 0$, plotting Q_1 at each intersection). If X_n is the nth intersection of the orbit with the section then X_{n+i} is the $(n+i)$th intersection for an integer i [28]. The plots for a range of forcing frequencies are shown in Figures 4.5 and 4.6. The first 3 plots show the periodic solution for the 2 attractors. Plots (a) and (c) in Figure 4.5 are from branch A3 in Figure 4.2(b) with plot (b) coming from branch A6. The 2 attractors persist into the chaotic region. Plots (e), (i) and (l) of Figure 4.5 and plots (a)-(g) of Figure 4.6 are from branch A6 with the rest coming from branch A3. The first thing to note is that the size of the attractor is increasing as the forcing frequency increases, suggesting the two attractors are created at around the same point at a lower forcing frequency than can be followed. The other interesting feature of the attractors is that the solution does not become completely chaotic straight away. There is a gradual decline in structure as the forcing frequency increases. Plot (i) of Figure 4.5 is a good example of the structure of the quasi-periodic solution at a forcing frequency of $\omega = 8944$. There appears to be a phase-locking of the nonperiodic solution. The trajectory is close to becoming period-nine as shown in Figure 4.7, a delay plot of nine iterates. The nonperiodic attractor approximately aligns along the $X_{n+9} = X_n$ line. The shape of the attractors approach that of a square-root mapping with an infinite gradient relative to the $X_{n+9} = X_n$ line. This is typical of impacting systems with grazing.

The quasi-periodic period-nine attractor is illustrated clearly for a higher forcing frequency of $\omega = 9212$ in Figure 4.8. The figure plots the angle in phase space between Q_1 and Q_2 at a Poincaré section created by taking the states of the system at equal time intervals defined by one period of the forcing frequency. The structure of the chaotic attractor suggests there might have been grazing of an invariant torus. The analysis of grazing bifurcations of invariant tori has not yet been done however we refer to [7, 9, 32] for examples of other systems that have similar properties to those shown here. The grazing of this torus is an area of future investigation.

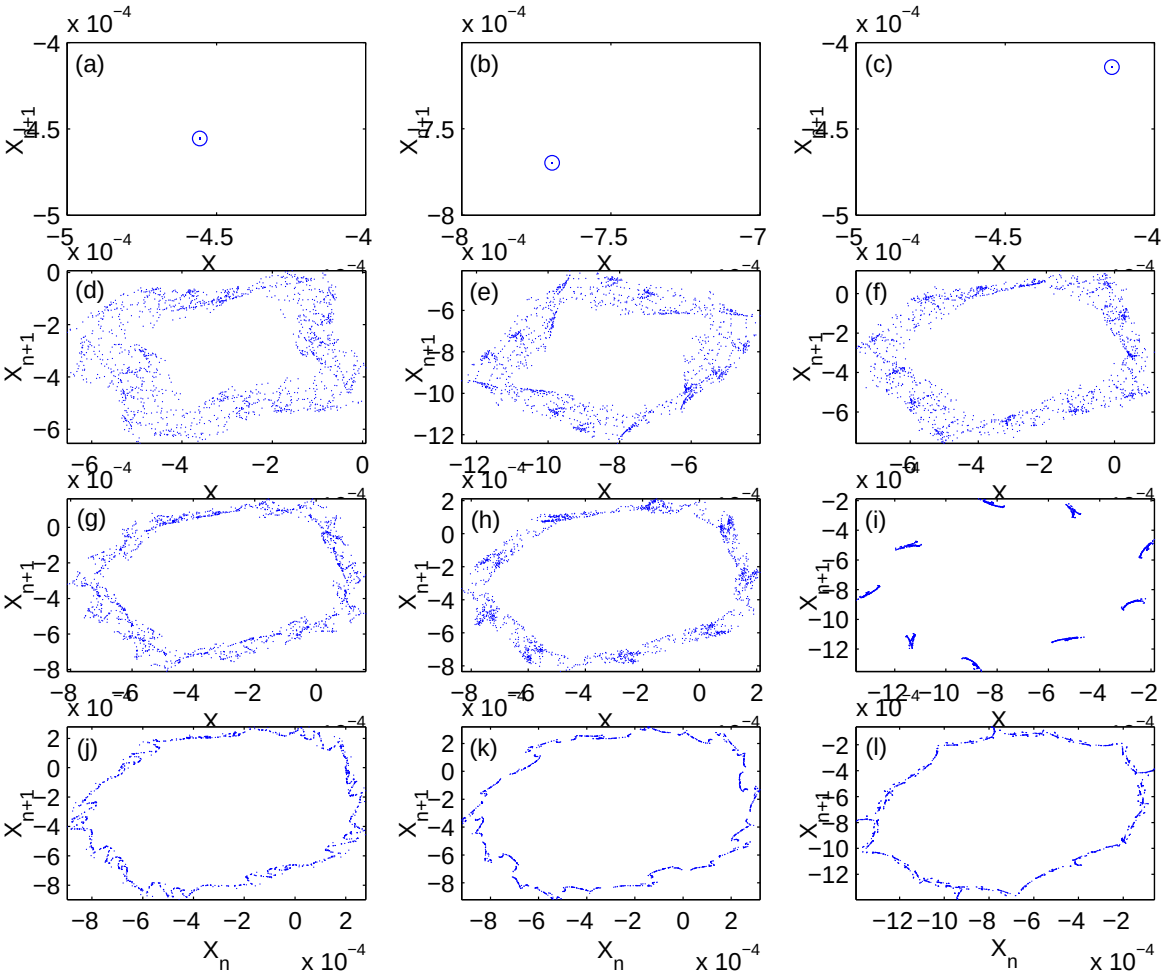

FIG. 4.5. *Delay plots for the Poincaré section Σ of a series of forcing frequencies ω as (a)8228.7, (b)8318.2, (c)8407.6, (d)8497.1, (e)8586.5, (f)8675.9, (g)8765.4, (h)8854.8, (i)8944.3, (j)9033.7 (k)9123.2, (l)9212.6.*

5. Conclusion. The main result from this paper is that a nonlinear damper can introduce undesirable dynamics in an otherwise linear system. The main cause of such dynamics are the valves (see Figure 2.1). The trajectories of the valves can significantly affect the response of the whole system. Of particular interest is the effect of the valves when they impact the valve seats. It has been shown that the system can undergo qualitatively different dynamics depending on whether the valves impact or not. At the point where the valves just impact we find a grazing bifurcation. Many unstable solutions exist on one side of the bifurcation: infinitely many trajectories where the valve impacts on the valve seat and one trajectory where the valve does not impact the seat. The two sets of solutions annihilate each other at the grazing point. We have presented a detailed analysis of the simplest two grazing bifurcations in this system and argued that the grazing of the period-two orbit is responsible, in some sense, for the birth of a chaotic attractor. There are three points where chaotic

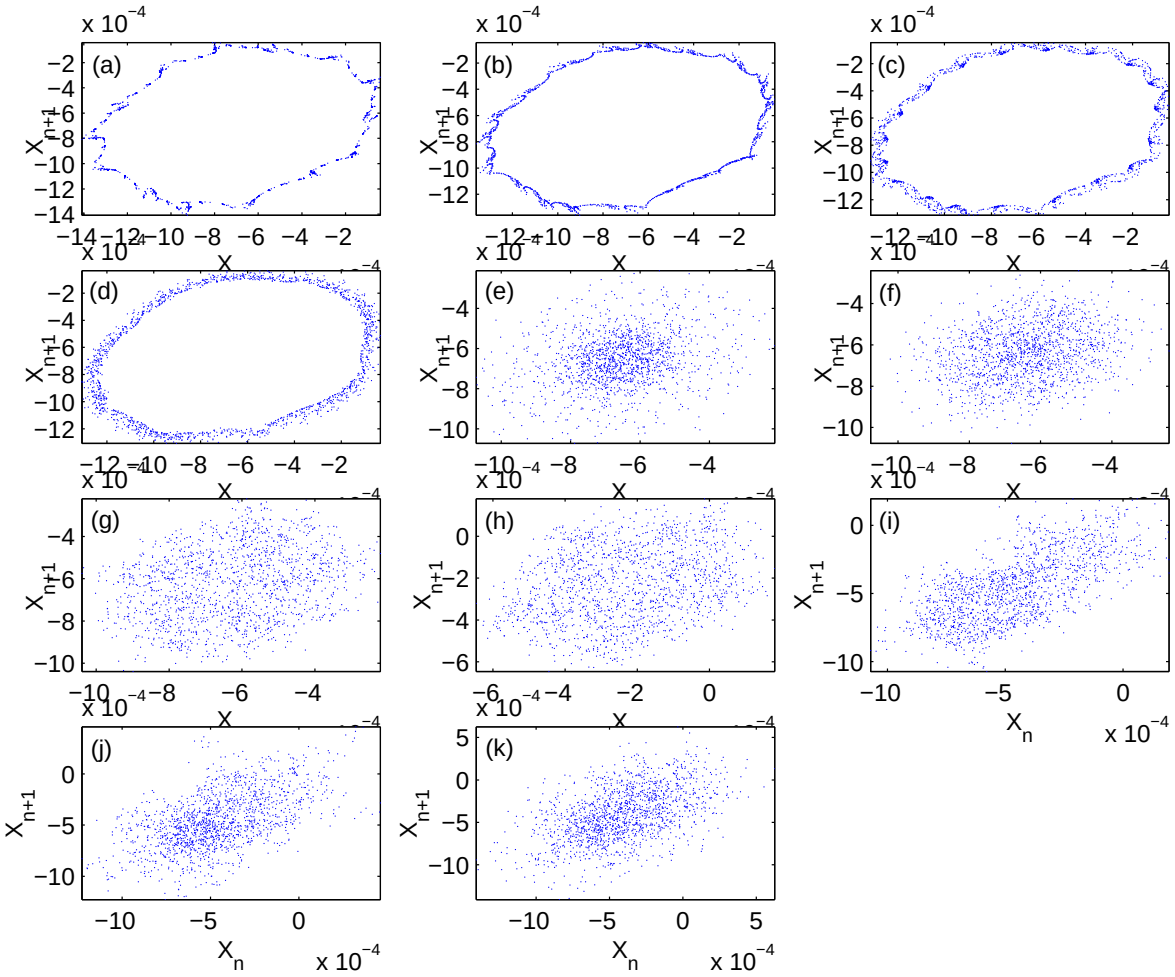

FIG. 4.6. *Delay plots for the Poincaré section Σ of a series of forcing frequencies ω as (a)9302.0, (b)9391.5, (c)9480.9, (d)9570.4, (e)9659.8, (f)9749.3, (g)9838.7, (h)9928.1, (i)10018, (j)10107, (k)10196.*

attractors are born. There are two standard grazing bifurcations at $\omega = 8000$ and 9414 and one point where a quasi-periodic attractor is born due to the grazing of a torus. To the knowledge of the authors this is the first time this kind of bifurcation has been studied in such a complex system as the damper examined in this paper.

None of this analysis would have been possible without the dedicated numerical method. A more general continuation algorithm for piecewise-smooth systems would be desirable to fully analyse the system. A report from SICONOS (SImulation and COntrol of NOnsmooth dynamical Systems) [3] takes the first steps in this direction. Of specific interest is the grazing of the quasi-periodic torus and treatment of its mode-locking. To progress in this area, the discontinuity mappings should be derived which can become complicated for large systems such as the one studied in this paper.

It is important to understand why non-periodic orbits exist so that they can be avoided when using the damper in a larger system. For instance a non-periodic motion

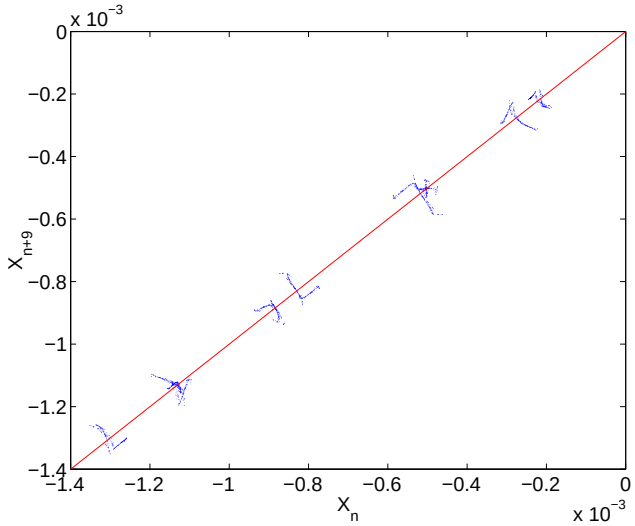

FIG. 4.7. *Delay plots of Q_1 for the Poincaré section Σ $Q_2 = 0$ for ω =8944. Plotting a delay of 9 intersections with a line $X_n = X_{n+9}$ for reference.*

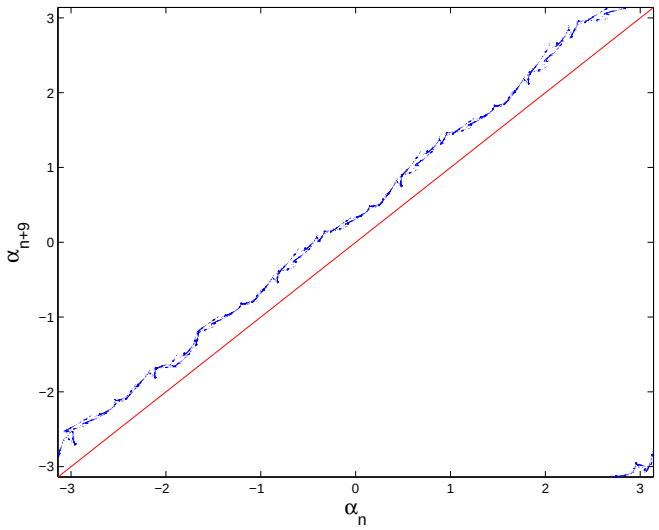

FIG. 4.8. *Delay plots for the angle between Q_1 and Q_2 at ω =9212. Plotting a delay of 9 intersections with a line $\alpha_n = \alpha_{n+9}$ for reference.*

of the system's mass could lead to high vibrations, causing unpredictable fatigue that would reduce the life of the system. A periodic response from the mass would still cause vibrations, however these can be more easily predicted, and thus the life of the structure can be calculated and possibly lengthened.

Acknowledgments. R.D. Eyres would like to acknowledge the support of CASE award (01305192) from Westland Helicopters Ltd. and EPSRC. P.T. Piiroinen would like to acknowledge the support of the EU FP5 Project SICONOS (IST-2001-37172).

REFERENCES

[1] J. Adolfsson, H. Dankowicz and A. Nordmark, *3D passive walkers: Finding periodic gaits in the presence of discontinuities*, Nonlinear Dynamics, 24 (2001), pp. 205-229.

[2] M. di Bernardo, C. J. Budd, and A. R. Champneys, *Grazing bifurcations in n-dimensional piecewise-smooth dynamical systems*, Physica D, 160 (2001), pp. 222-254

[3] M. di Bernardo, C. Budd, A. Champneys, P. Kowalczyk, A. Nordmark, G. Olivar, P. Piiroinen, *SICONOS deliverable WP4.1: A review of codimension-one nonsmooth bifurcations*, Technical report, in submission (2004).

[4] A. Blakeborough, *An analytical response of church bells to earthquake exitation*, Journal of Earthquake Engineering, 5 (2001), pp. 69-92.

[5] C. Budd, F. Dux and A. Cliffe, *Effect of frequency and clearance variations on single-degree-of-freedom impact oscillators*, Journal of Sound and Vibration, 184 (1995), pp. 475-503.

[6] D. R. J. Chillingworth, *Discontinuity geometry for an impact oscillator*, Dynamical Systems, 17 (2002), pp. 389-420.

[7] H. J. Dankowicz, P. T. Piiroinen and A. B. Nordmark, *Grazing bifurcations of initially quasi-periodic system atttractors*, Proceedings of the ASME Design Engineering Technical Conference, 6 (2001), pp. 1189-1195.

[8] H. J. Dankowicz and P. T. Piiroinen, *Exploiting discontinuities for stabilization of recurrent motions*, Dynamical Systems, 17 (2002), pp. 317-342.

[9] H. J. Dankowicz, P. T. Piiroinen and A. B. Nordmark, *Low-velocity impacts of quasiperiodic oscillations*, Chaos, Solitons and Fractals, 14 (2001), pp. 241-255.

[10] M. A. Dokainish and M. M. Elmadany, *On the non-linear response of a relief valve*, ASME Journal of Mechanical Design, 100 (1978), pp. 675-680.

[11] R. D. Eyres, A. R. Champneys and N. A. J. Lieven, *Modelling and Dynamic Response of a Damper with Relief Valve*, Nonlinear Dynamics, (2004), to appear.

[12] M. H. Frederiksson and A. B. Nordmark, *On normal form calculations in impact oscillators*, Proc. Royal Soc. Lond. A, 456 (2000), pp. 315-329.

[13] G. W. Housner, L. A. Bergman, T. K. Caughey, A. G. Chassiakos, R. O. Claus, S. F. Masri, R. E. Skelton, T. T. Soong, B. F. Spencer and J. T. P Yau, *Structural engineering: past, present and future*, Journal of Engineering Mechanics, 123 (1997), pp. 117–134.

[14] H. H. Lang, *A Study of the characteristics of automotive hydraulic dampers at high stroking frequencies*, Ph.D. thesis, Department of Mechanical Engineering, University of Michigan, 1997.

[15] R. I. Leine, *Bifurcations in Discontinuous Mechanical Systems of Filippov-Type*, Ph.D. thesis, Teknische Universiteit Eindhoven, The Netherlands 2000.

[16] Mathworks Inc, *MATLAB version 6.1*, 2001.

[17] P.C. Müller, *Calculation of Lyapunov Exponents for dynamical systems with discontinuities*, Chaos, Solitons and Fractals, 5 (1995), pp. 1671-1681.

[18] A. H. Nayfeh and B. Balachandran, *Applied Nonlinear Dynamics: Analytical, Computational, and Experimental Methods*, John Wiley and Sons, Inc., 1995.

[19] A. B. Nordmark, *Non-periodic motion caused by grazing incidence in an impact ocsillator*, Journal of Sound and Vibration, 145 (1991), pp. 279-297.

[20] A. B. Nordmark, *Existence of periodic orbits in grazing bifurcations of impacting mechanical oscillators*, Nonlinearity, 14 (2001), pp. 1517-1542.

[21] F. Peterka, *Bifurcations and transition phenomena in an impact oscillator*, Chaos, Solitons and Fractals, 7 (1996), pp. 1635-1647.

[22] P. T. Piiroinen, *Recurrent Dynamics of Nonsmooth Systems with Application to Human Gait*, Ph.D. thesis, Department of Mechanics, Royal Institute of Technology, Stockholm, 2002.

[23] P. T. Piiroinen, L. N. Virgin and A. R. Champneys, *Chaos and Period-Adding; Experimental and Numerical Verification of the Grazing Bifurcation*, Journal of Nonlinear Science, 14(2004), pp. 383-404.

[24] A. A. Seleemah and M. C. Constantinou, *Investigation of seismic response of buildings with linear and nonlinear fluid viscous dampers*, National Centre for Earthquake Engineering Research, Technical report NCEER-97-0004 (1997).

[25] S. H. Strogatz, *Nonlinear Dynamics and Chaos*, Perseus Books, 1994.

[26] C. Surace, K. Worden and G. R. Tomlinson, *An improved nonlinear model for an automotive shock absorber*, Nonlinear Dynamics, 3 (1992), pp. 413-429.

[27] C. Surace, K. Worden and G. R. Tomlinson, *On the nonlinear characteristics of automotive shock absorbers*, Proceedings of the Intsitute of Mechanical Engineers Part D: Journal of Automobile Engineering, 206 (1992), pp. 1-16.

[28] L. N. Virgin, *Introduction to Experimental Nonlinear Dynamics*, Cambridge University Press, Cambridge, 2000.
[29] J. Wallaschek, *Dynamics of non-linear automobile shock absorbers*, International Journal of Non-Linear Mechanics, 25 (1990), pp. 299-308.
[30] G. S. Whiston, *Global dynamics of a vibro-impacting linear oscillator*, Journal of Sound and Vibration, 118 (1987), pp. 395-429.
[31] G. S. Whiston, *Singularities in vibro-impacting dynamics*, Journal of Sound and Vibration, 152 (1992), pp. 427-460.
[32] Z. T. Zhusubaliyev and E. Mosekilde, *Bifurcations and Chaos in Piecewise-Smooth Dynamical Systems*, World Scientific Publishing Co. Pte. Ltd., Singapore, 2003.

Appendix A. Existence conditions of periodic orbits from a grazing point. A set of conditions have been derived by Nordmark [3, 20] that define the existence of periodic orbits being created at a grazing point. The state is given by x and the bifurcation parameter is denoted as μ to apply to (2.14) in this paper.

Here we will summarise the conditions derived by Nordmark in a nontechnical way and a form that can be directly applied to (2.14). The N-dimensional system $\dot{x} = f(x, \mu)$, where $N = 8$, will be used to determine which periodic orbits are created or destroyed at a grazing bifurcation.

We suppose there is a non-impacting periodic orbit such that there is a Poincaré mapping of the smooth orbit near $x = 0$, $\mu = 0$ given as $x \to f(x, \mu)$ so $f(0, 0) = 0$. The Jacobian of the mapping will be

$$A = D_x f(0, 0),$$

where D_x is the first derivative with respect to x. The Jacobian calculation is not straightforward when a system encounters a discontinuity in one of the states and is discussed in detail in [22]. The first derivative of the system with respect to the bifurcation parameter at $f(0, 0)$ is denoted as M so

$$M = D_\mu f(0, 0).$$

The discontinuity will occur on a surface defined by the zero of a smooth function h (where $h(0, 0) = 0$) which has a negative value leading to a low-velocity impact and positive values for a non-impacting orbit such that

$$C = D_x h(0, 0).$$

A second mapping, g, is introduced to take into account this *jump* in state at the surface defined by h given as

$$g(x, \mu) = \begin{cases} x, & \text{if } h(x, \mu) \geq 0, \\ b(x, y, \mu)y + x, & \text{if } h(x, \mu) \leq 0, \end{cases} \tag{A.1}$$

where

$$y = \sqrt{-h(x, \mu)}, \tag{A.2}$$

to leading order for an impacting system [19], and b represents the jump in state at impact and is given by

$$b = \begin{bmatrix} 0 & 0 & 0 & (1 + r) & 0 & 0 & 0 \end{bmatrix}^T \sqrt{2a},$$

for the grazing of valve 2 in (2.14) where $a = \frac{dX_4}{dt}$ at the grazing point of the grazing orbit. The quantity b is smooth and is referred to as B about the zero as

$$B = b(0, 0, 0) \neq 0.$$

In the generic case a periodic point $\overline{x}$ of period n can be described by

$$\overline{x} = (g \circ f)^n(\overline{x}, \mu) \tag{A.3}$$

but this can cause problems due to the choice of g and singularities in the derivative at $h = 0$. We therefore define a periodic orbit with m impacts as a sequence

$(n_1, n_2, ..., n_m)$ of $n_1 - 1$ non-impacting iterates followed by a single impact followed by $n_2 - 1$ non-impacts etc. The total period is therefore given by $n = \sum_{i=1}^{m} n_i$. The aim is to define the existence of a periodic orbit with a given impacting sequence. A period-one impacting orbit can then be described by n_1 only with $n_1 = 1$. The state and value of y of the system at impact i is denoted as x_i and y_i respectively so a fixed point (periodic orbit) is given as $\overline{x} = x_1$. A non-impacting fixed point of period n satisfies

$$\overline{x} - f^n(\overline{x}, \mu) = 0 \tag{A.4}$$

restricted by

$$h(f^k(\overline{x}, \mu), \mu) > 0 \text{ for } 1 \leq k \leq n. \tag{A.5}$$

An impacting sequence defined by the notation above $(n_1, n_2, ..., n_m)$ is given by the set of equations

$$\begin{gathered} x_2 - b(f^{n_1}(x_1, \mu), y_1, \mu)y_1 - f^{n_1}(x_1, \mu) = 0 \\ h(f^{n_1}(x_1, \mu)) + y_1^2 = 0 \\ \vdots \\ x_1 - b(f^{n_m}(x_m, \mu), y_m, \mu)y_m - f^{n_m}(x_m, \mu) = 0 \\ h(f^{n_m}(x_m, \mu)) + y_m^2 = 0 \end{gathered} \tag{A.6}$$

subject to the condition for non-impacting iterates as (A.5)

$$h(f^k(\overline{x}, \mu), \mu) > 0 \text{ for } 1 \leq k \leq n_i - 1, \tag{A.7}$$

since n_i represents the impacting iterate, and

$$y_i > 0. \tag{A.8}$$

This set of equations and conditions define the periodic orbit with a given impact sequence. The iterate equations (A.6) can be linearised and put into matrix form together with the linearised definition of the impact surface (A.2).

Now let us consider the conditions (A.7) and (A.8). The direction of the variation in the bifurcation parameter should be taken into account. To make this clearer let us consider a small variation in one parameter μ about a fixed point $\widetilde{x}(\mu)$ of the above system ensuring the condition $\widetilde{x}(0) = 0$. This condition holds by the implicit function theorem if

$$\det(I - A) \neq 0 \tag{A.9}$$

where I is the identity matrix and

$$\widetilde{x}(\mu) = f(\widetilde{x}(\mu), \mu). \tag{A.10}$$

It will be assumed that the fixed point will cross $h = 0$ transversally for a change in μ. The aim is to find a simple expression, expressed in terms of μ, for a perturbation in μ about the fixed point. The coordinate system can then be changed according to this change in μ to yield a simplified system of equations and conditions. The resulting system and conditions from (A.6)-(A.8) will then contain information about

the direction of the perturbation and can therefore define which side of the grazing point the solution will exist. The first step is to perturb h as

$$h(\widetilde{x}(\mu),\mu) = h(0,0) + \frac{d}{d\mu}[h(\widetilde{x}(\mu),\mu)]\mu + \mathcal{O}(\mu^2) \tag{A.11}$$

since $h(0,0) = 0$ and expanding we find

$$h(\widetilde{x}(\mu),\mu) = \left(h_x \frac{d\widetilde{x}(\mu)}{d\mu} + h_\mu\right)\mu + \mathcal{O}(\mu^2). \tag{A.12}$$

Differentiating (A.10) with respect to μ

$$\frac{d\widetilde{x}(\mu)}{d\mu} = f_x \frac{d\widetilde{x}(\mu)}{d\mu} + f_\mu \tag{A.13}$$

so

$$(I - f_x)\frac{d\widetilde{x}(\mu)}{d\mu} = f_\mu \tag{A.14}$$

which is used in (A.12) to yield

$$h(\widetilde{x}(\mu),\mu) = \left(h_x(I - f_x)^{-1} f_\mu + h_\mu\right)\mu + \mathcal{O}(\mu^2). \tag{A.15}$$

so

$$h(\widetilde{x}(\mu),\mu) = e\mu + \mathcal{O}(\mu^2) \tag{A.16}$$

where

$$e = D_\mu(h(\widetilde{x}(\mu),\mu))(0) = C(I - A)^{-1}M + (D_\mu h)(0,0) \neq 0. \tag{A.17}$$

The system of equations can be summarised in matrix form using

$$z = \begin{bmatrix} x_1 & y_1 & \cdots & x_m & y_m \end{bmatrix}^T$$

so (A.6) can be expressed as $F(z,\mu) = 0$ with solution $F(0,0) = 0$. The solution $z(\mu)$ from $z(0) = 0$ is defined uniquely by the implicit function theorem if $(D_z F)(0,0)$ is nonsingular and (A.7) and (A.8) hold.

As suggested above, the system of equations (A.6)-(A.8) can be rescaled with the offset from the fixed point as $x = \widetilde{x}(\mu) + e\mu\chi$, $y = e\mu Y$. The solution can then be described as

$$Z = \begin{bmatrix} \chi_1 & Y_1 & \cdots & \chi_m & Y_m \end{bmatrix}^T.$$

A period-k non-impacting sequence as in (A.3) can now be rewritten as

$$f^k(x,\mu) = f^k(\widetilde{x}(\mu) + e\mu\chi,\mu)$$

which gives, on expansion with (A.10),

$$f^k(x,\mu) = f^k(\widetilde{x}(\mu),\mu) + f_x^k e\mu\chi + \mathcal{O}(\mu^2) = \widetilde{x}(\mu) + e\mu A^k\chi + \mathcal{O}(\mu^2). \tag{A.18}$$

Expressing (A.16) in terms of the new coordinates and the definition of the fixed point we get

$$h(f^k(x,\mu),\mu) = h(\widetilde{x}(\mu) + e\mu A^k\chi + \mathcal{O}(\mu^2),\mu)$$

so with (A.16)

$$h(f^k(x,\mu),\mu) = h(\widetilde{x}(\mu),\mu) + h_x e\mu A^k\chi + \mathcal{O}(\mu^2) = e\mu + e\mu CA^k\chi + \mathcal{O}(\mu^2). \tag{A.19}$$

Taking the first line of (A.6) with (A.18) and (A.19) with the substitutions $x_2 = \widetilde{x}(\mu) + e\mu\chi_1$ and $y_1 = e\mu Y_1$

$$\widetilde{x}(\mu) + e\mu\chi_1 - Be\mu Y_1 - (\widetilde{x}(\mu) + e\mu A^k\chi_1) + \mathcal{O}(\mu^2) = 0$$

and the second line of (A.6) yields

$$e\mu + e\mu CA^k\chi_1 + \mathcal{O}(\mu^2) = 0.$$

Similar expressions for the rest of the impacting sequence can be derived and put into matrix form. For the impacting sequence $(n_1, n_2, ..., n_m)$ the matrix $(D_zF)(0,0)$ is defined as the banded structure $D_{(n_1,n_2,...,n_m)}$. For $m = 3$

$$D_{(n_1,n_2,n_3)} = \begin{bmatrix} -A^{n_1} & -B & I & 0 & 0 & 0 \\ CA^{n_1} & 0 & 0 & 0 & 0 & 0 \\ 0 & 0 & -A^{n_2} & -B & I & 0 \\ 0 & 0 & CA^{n_2} & 0 & 0 & 0 \\ I & 0 & 0 & 0 & -A^{n_3} & -B \\ 0 & 0 & 0 & 0 & CA^{n_3} & 0 \end{bmatrix}. \tag{A.20}$$

The system can then be written as

$$D_{(n_1,n_2,...,n_m)}Z(\mu) = \begin{bmatrix} 0 \\ -1 \\ \vdots \\ 0 \\ -1 \end{bmatrix} + \mathcal{O}(\mu), \tag{A.21}$$

with the conditions

$$\text{sign}(e\mu)(CA^k\chi_i(\mu) + 1) + \mathcal{O}(\mu) > 0 \text{ for } 1 \le k \le n_i - 1 \tag{A.22}$$

and

$$\text{sign}(e\mu)Y_i(\mu) > 0 \tag{A.23}$$

derived as above for (A.7) and (A.8) respectively and dividing by the modulus of $e\mu$ to preserve the dependence on the sign of $e\mu$.

The set of equations defined by (A.21) can then be solved for Z. A solution with impacting sequence $(n_1, n_2, ..., n_m)$ exists for small μ for either $\mu = 0+$ or $\mu = 0-$ if (A.22) and (A.23) hold for the solution to (A.21), with conditions $\det(I - A) \neq 0$, $e \neq 0$ and $\det(D_{(n_1,...,n_m)}) \neq 0$. If any expression on the left hand side of (A.22) or (A.23) are negative then no solution exists for that sequence of impacts.

The side of the grazing point that these orbits exist is of interest as we wish to predict the direction of the branches from the bifurcation. As the bifurcation parameter μ changes across the grazing point, the sign of μ will change. The term e can be taken to be a constant so the left hand side of the conditions (A.22) and (A.23) will change sign. This change in sign results in the conditions no longer holding and so the orbit can only exist on one side of the bifurcation.

The direction of the impacting orbits can be determined by considering the non-impacting orbits and the solution to the system in (A.21). As an example let us take the case of a period-one orbit. The system in (A.21) can be written as

$$(I - A)\chi_1 - BY_1 = 0,$$

$$CA\chi_1 = -1.$$

Rearranging these equations and converting back into the original coordinates with $y = e\mu Y$ yields

$$y_1 = -\frac{e\mu}{CA(I - A)^{-1}B}$$

and using the notation for a general period-n orbit

$$s(n) = CA^n(I - A^n)^{-1}B \tag{A.24}$$

produces

$$y = -\frac{e\mu}{s(1)} > 0 \tag{A.25}$$

for a period-one orbit, noting $y > 0$ as (A.8).

A non-impacting orbit is defined by the condition in (A.5). Using the derived form of h in (A.16) we can state that for a non-impacting orbit (so $h > 0$)

$$h(x, \mu) = e\mu > 0,$$

so the sign of the quantity $e\mu$ is $+1$. It follows that if the constant e at or close to the grazing point is positive then the direction of the non-impacting orbit will be defined by $\mu > 0$. The converse argument holds for $e < 0$ so $\mu < 0$.

For the impacting period-one orbit $h < 0$, so if s(1)< 0 then $e\mu > 0$ for the orbit to exist, as defined by (A.25). In the example where e is positive, the result indicates that the period-one impacting orbit will be on the *same side* as the non-impacting orbit because μ must be positive.

The above argument can be applied to any given impacting sequence. If all the conditions in (A.22) and (A.23) are of the same sign and positive for a given impacting sequence then the orbit exists on the same side of the non-impacting orbit relative to the grazing point. If the conditions are all of the same sign but negative then the orbit exists on the opposite side to the non-impacting orbit. In contrast, if the conditions (A.22) and (A.23) are of both signs for a particular orbit sequence $(n_1, n_2, ..., n_m)$ then no periodic orbit of that type can be either created or destroyed in the bifurcation.